Heliyon 9 (2023) e19438

Contents lists available at ScienceDirect

Heliyon

journal homepage: www.cell.com/heliyon

Investigations on the thermoelectric and thermodynamic properties of quaternary coinage metal HgSBr

Hariharan M, Eithiraj R.D *

Division of Physics, School of Advanced Sciences, Vellore Institute of Technology (VIT), Chennai, 600127, Tamil Nadu, India

ARTICLE INFO

Keywords:
Chalcogenide halides
DFT
Narrow band gap
Elastic properties
Lattice thermal conductivity
Exciton binding energy

ABSTRACT

We present the findings of a thorough first-principles analysis of physical parameters related to the ground state, elastic, electronic, optical, thermodynamic, and transport properties of the quaternary coinage metal-based compound CuHgSBr using the WIEN2k package. The computed equilibrium lattice parameters align well with their experimental equivalents, providing strong support for the validity of the findings. We performed numerical and computational calculations to estimate the elastic constants for the orthorhombic structure with space group *Pbam*. The band structure analysis of CuHgSBr reveals an indirect band gap semiconductor of 0.76 eV, classifying it as a p-type semiconductor. We also calculated the optical properties within the energy range of 0–13.56 eV. Moreover, we investigated the effective mass, exciton binding energy, and exciton Bohr radius, which indicated that CuHgSBr exhibits a weak exciton binding energy and belongs to the Mott-Wannier type exciton category. Using the Boltzmann transport theory, along with the constant relaxation time and Slack equations, we determined the thermoelectric properties and lattice thermal conductivity of CuHgSBr. Notably, the figure of merit at 800 K is calculated to be 0.54, which is encouraging for potential thermoelectric applications. The comprehensive research study we conducted provides valuable insights for experimental research across multiple physical properties, as the material is being theoretically examined for the first time in this full prospectus.

1. Introduction

Around the world, active research is being conducted in the hunt for effective materials for use in photovoltaics, optoelectronics and thermoelectric devices. Waste heat causes a significant loss of useable energy, with this lost heat being of excellent quality but dispersed. As the need for electricity among humans continues to grow, sustainable energy-producing techniques like thermoelectric energy generation are becoming increasingly crucial [1]. The discovery made by Seebeck in 1821 revealed that thermoelectric (TE) materials have the capability to produce power by utilizing a difference in temperature, which is known as the Seebeck effect. Conversely, the Peltier effect generates a temperature difference using electricity. As a result, there is a need for thermoelectric materials with exceptional performance to efficiently transform heat into electric energy on a continuous basis [2,3].

In recent times, the exploration of high-performance thermoelectric substances has garnered increasing attention from the fields of energy and the environment, driven by the prospect of potential commercial applications. The complexity of thermoelectric materials at the structural, electrical, and compositional levels necessitates close collaboration among a broad scientific community consisting of chemists, physicists, and materials scientists [4–6]. Notably, spacecraft have been continuously utilizing this energy-generating

* Corresponding author.
E-mail address: eithiraj.rd@vit.ac.in (E. R.D).

https://doi.org/10.1016/j.heliyon.2023.e19438
Received 26 April 2023; Received in revised form 22 August 2023; Accepted 22 August 2023
Available online 25 August 2023

technique since early 1960s [7,8]. For the past two decades, thermoelectric materials have been at the forefront of research aimed at utilizing waste heat in stationary applications and automobiles to reduce the burden on alternators [9].

Several organisations have led the way in global-scale thermoelectric development, with numerous significant advancements made possible by fundamental insights based on first-principles. The DFT framework enables the estimation of band structure projections, phase diagrams through cluster expansion techniques, and phase stability of unidentified compounds. Over the past 15 years, the thermoelectric figure of merit (ZT) of half-Heusler alloys, fascinating class of thermoelectric materials, has experienced significant improvement. Recently, there has been a notable interest in chalcogenide materials for narrow/wide bandgap semiconductors, which are frequently employed in optoelectronic devices. Photovoltaic technology relies on a variety of materials, including primarily organic, inorganic, or organic-inorganic mixtures, for efficient photon-to-electron conversion [10].

Recent experimental and theoretical reports have highlighted several ternary and quaternary chalcogenide-based materials [11–15] for optoelectronics [16–20] and thermoelectric [21–26] applications. Consequently, we conducted DFT computation on the quaternary chalcogenide-based material CuHgSBr, which has demonstrated extraordinarily high efficiency and provides a fundamental overview of all digital tools. The synthesis involves a hydrothermal reaction within sealed glass ampoules at 670 K, yielding yellow-orange CuHgSBr crystals. The most prevalent crystal structure for our chemical is orthorhombic with space group *Pbam*. The structures comprise flattened HgS chains that are interconnected by a combination of distorted CuS_2Br_2 tetrahedra sharing an edge with Br atoms. Notably, the copper atoms are positioned off-centre, as corroborated by experimental investigations [27]. The prior structural method, reliant on powder diffraction data [28], was invalidated upon the determination of a single crystal structure. The structural archetype of CuHgSBr bears a striking resemblance to previously identified compounds like CuHgSeBr, AgHgSBr, AgHgSI (collectively known as MHgYX) [29].

In the current work, we employed the comprehensive full potential linearized augmented plane wave (FP-LAPW) technique using the WIEN2k software to analyze the structural, elastic, electronic, and optical aspects of CuHgSBr. We are not aware of any literature describing the structural, transport, electronic, optical, thermodynamic, and elastic properties of these materials.

2. Computational details

The DFT computation were performed for the quaternary compound CuHgSBr to estimate its ground state, electronic behavior, elasticity, optical and transport characteristics. We used the WIEN2k [30] package to calculate all these properties. To achieve this, we employed the WIEN2k software [30], utilizing the Generalized Gradient Approximation (GGA) with the Perdew-Burke-Ernzerhof (PBE) method [31] to account for electron exchange-correlation effects. For CuHgSBr, we set an energy separation of −6.0 Ry between the valence and core states. The parameters R_{MT} x K_{max} were chosen as 8.0, with a k value of $4 \times 4 \times 4$ using Monkhorst-Pack method. Notably, 2000 k points were designated solely for optical property calculations. Muffin tin radii, which prevent core charge leakage, were set at 2.19, 2.44, 1.79, and 2.14 for Cu, Hg, S, and Br, respectively. The calculations for CuHgSBr's structure were based on lattice constants reported experimentally [27]. To analyze structural parameters and their dependence on energy against the c/a ratio, Murnaghan's state equation was employed. The determination of elastic constants was facilitated by the IR-Elast package [32], integrated within the WIEN2k code, leading to the assessment of various elastic parameters. Optical properties were explored through the complex dielectric function, while transport properties were studied using the BoltzTraP code [33].

3. Results and discussion

3.1. Geometry optimization

The quaternary compound CuHgSBr exhibits an orthorhombic crystal structure with the *Pbam* space group and Brillouin zone plot, as shown in Fig. 1(a) and (b). Structural optimization was executed using the reported experimental lattice parameters [27]. The total

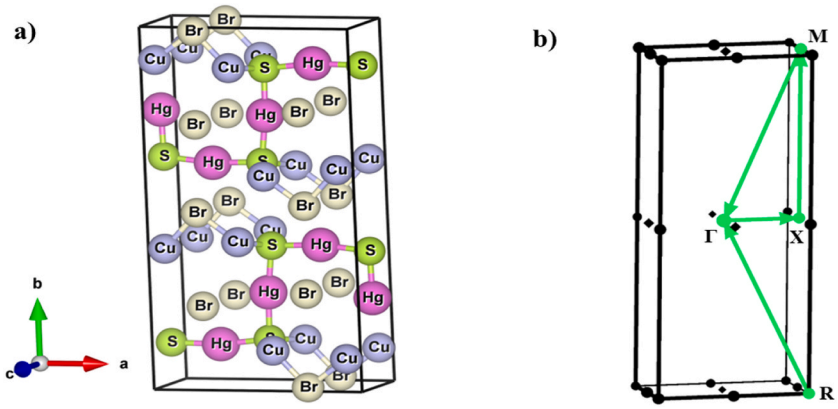

Fig. 1. a) Crystal structure of CuHgSBr, and b) First Brillouin zone representing high symmetry k points for CuHgSBr compound.

energy was fitted into the Murnaghan equation of state as a function of c/a, and this relationship was visualized in Fig. 2. Based on the total energy vs c/a ratio, the optimized lattice parameters, total energy and equilibrium volume for different functionals were computed and listed in Table 2. Among the exchange-correlation functionals considered, GGA-PBE exhibited the lowest ground state energy, as indicated by the obtained total energy values. Consequently, GGA-PBE was selected as the functional for computing all the physical properties discussed in this paper. Our computed outcomes demonstrated favorable consistency with experimental data. Furthermore, we determined the bond lengths for CuHgSBr, and these values are detailed in Table 1.

3.2. Electronic properties

The energy dispersion within CuHgSBr defines its electronic characteristics, a feature elucidated by the calculated band structure presented in Fig. 3. This band structure assessment is conducted across significant directions within the Brillouin zone, highlighting high-symmetry paths. The valence band maximum (VBM) and conduction band minimum (CBM) predominantly consist of Cu-*d* and S-*p* states, respectively. Notably, the material possesses an indirect narrow band gap of 0.76 eV, determined through the application of the PBE-GGA method. The CBM is situated at the high-symmetry gamma point, while the VBM resides between the R and Γ points, indicative of an asymmetrical location. Fig. 1(b), portrays the first Brillouin zone alongside high-symmetry k paths. The presence of non-symmetrical points within the band structure holds promise for thermoelectric materials, a trait previously acknowledges in high-performance material studies [34–37].

We also estimated the band gap values using various exchange-correlation methods within the WIEN2k software, and these outcomes are listed in Table 2. Near the Fermi level E_F, the band structure shows very flat energy dispersion in the X-Γ direction, indicating a high hole effective mass. Flat bands, characterized by minimal energy dispersion, have significant effects on electronic properties and can lead to interesting physical phenomena, such as a high density of states, which enhances various electronic and transport properties, including thermoelectric efficiency.

The valence band region exhibits a collection of more dispersive flat bands and less dispersive parabolic bands. Flat bands find applications in 2D and 3D materials, such as ferromagnetism, superconductivity, Mott insulators, thermoelectric devices, quantum Hall effect, strongly correlated systems, Kagome lattice, and several topological states [38–49]. In our case, the presence of flat bands in the VB enhances the performance of thermoelectric devices, leading to an elevation in the Seebeck coefficient. All of these aspects are discussed in the transport properties section.

Regarding the conduction band (CB), there is only one band at the bottom, with an average effective mass of roughly 0.1 electrons, signifying the prevalence of electrons as the main charge carriers. The collective density of states (DOS) and partial density of states (PDOS) are shown in Figs. 4 and 5(a-d). The calculated S-*p* peak is at 1–3 eV below the CBM, and the Cu-*d* peak is at 0 to −3 eV. The lower VB is composed of Hg-*d* orbitals, while the higher VB closest to the Fermi level is made up of Cu-*d*, S-*p* and Br-*p* orbitals. S-*p* orbitals dominate the bottom of the CB, accounting to the primary significant peak in the CB DOS at 2 eV. The *s* states in the PDOS plots were neglected due to their deep energy level. It is important to note that there is currently no experimental research available for comparison regarding the electronic properties of CuHgSBr.

3.3. Elastic and mechanical properties

The ability of materials to regain their original size and shape after the stress within them is removed can be explained using elastic attributes, as long as the stress doesn't exceed the elastic limit. The mechanical traits of materials (represented by C_{ij}) are established by the elastic constants of single crystals. These constants are linked to the Debye temperature and Grüneisen parameter. The mechanical robustness of materials that are sought after for technological purposes, including factors like melting point, fracture

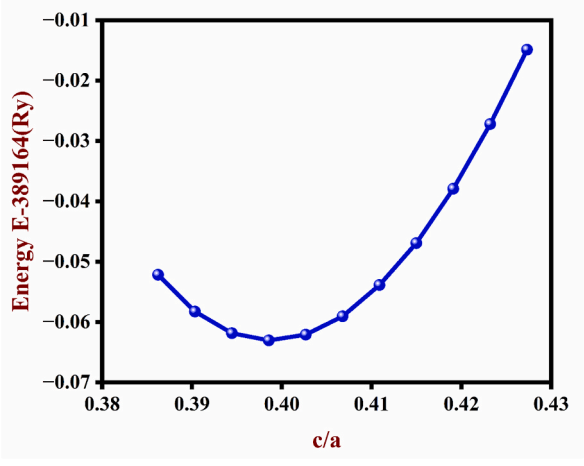

Fig. 2. Optimized c/a variations using GGA-PBE.

Table 1
Elucidated atomic bond lengths within the crystal structure of CuHgSBr.

Compound	Bond	Bond distance (Å)
CuHgSBr	Cu–Br	2.4553
	Hg–S	2.3799
	Cu–S	2.2817

Table 2
Calculated optimized lattice constants, equilibrium volume, band gap (eV) and total energy (Ry) using different exchange-correlation functional of CuHgSBr.

CuHgSBr	a (Å)	b (Å)	c (Å)	V (Å^3)	E_g (eV)	E_0 (Ry)
Experimental [27]	10.037	18.336	4.124	758.97	–	–
Theoretical (GGA-PBE)	10.137	18.517	4.042	758.71	0.767	−389164.053
GGA-WC	10.138	18.515	4.042	758.70	1.329	−389124.524
LDA	10.133	18.507	4.045	758.56	1.309	−388879.370
mBJ	–	–	–	–	1.243	−388874.601

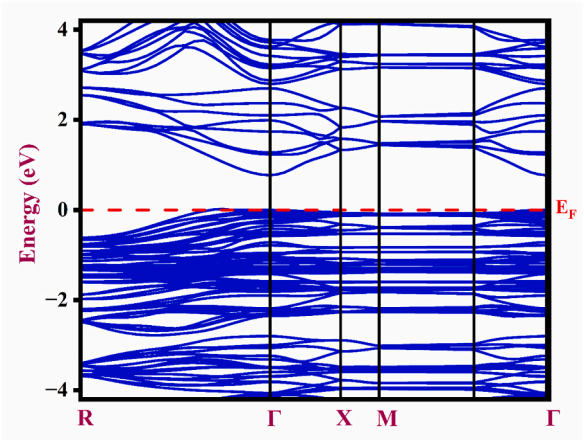

Fig. 3. Electronic band structure of CuHgSBr.

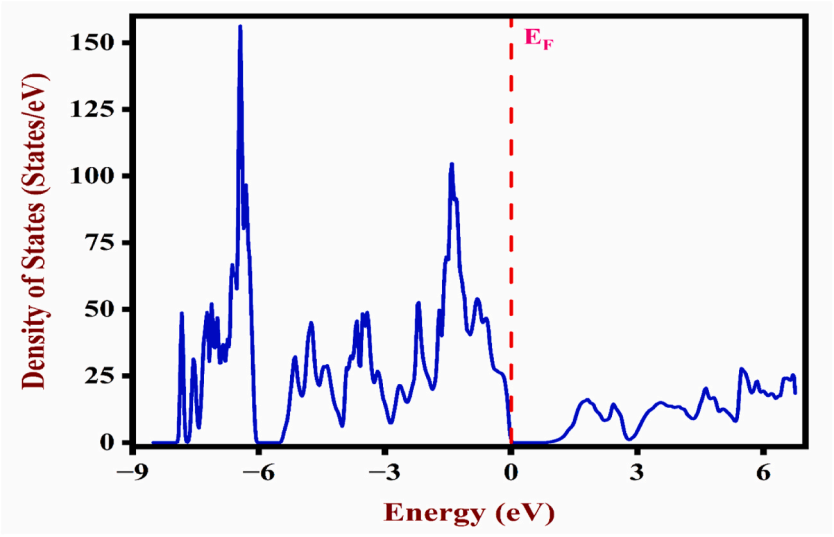

Fig. 4. TDOS of CuHgSBr.

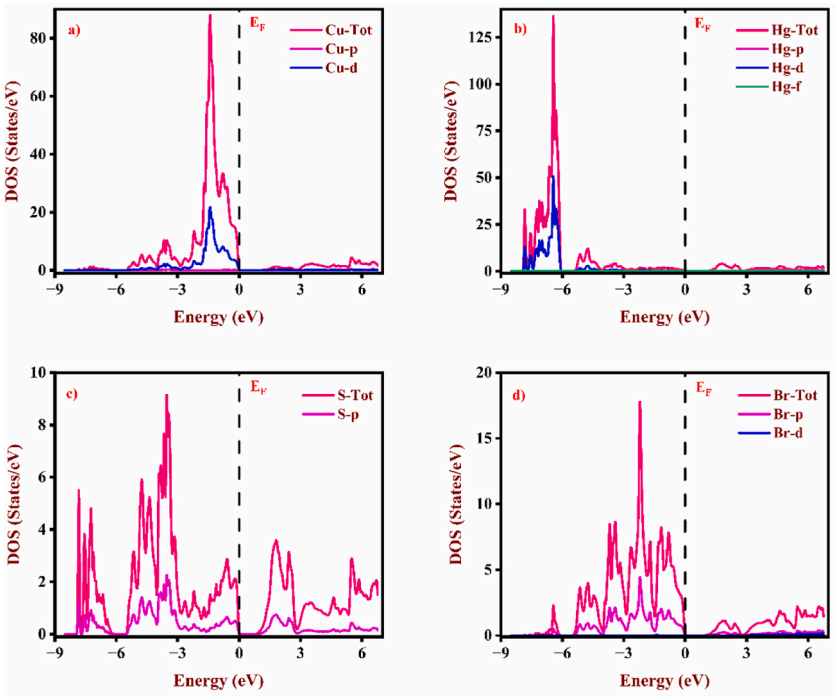

Fig. 5. PDOS for a) Copper (Cu), b) Mercury (Hg), c) Sulphur (S) and d) Bromine (Br).

toughness, load deflection, sound velocity, and thermoelastic stress, plays a significant role in their performance. These parameters also provide crucial insights into stiffness, material bonding, and the interatomic forces present within solids.

The CuHgSBr quaternary compound has an orthorhombic crystal structure [50], which is characterized by nine distinct elastic constants: C_{11}, C_{22}, C_{33}, C_{44}, C_{55}, and C_{66}, C_{12}, C_{13}, and C_{23}. These elastic constants must adhere to specific conditions (expressed in equations (1)–(7)) [51] to ensure the elastic stability of the orthorhombic crystal system, as defined by the Born-Huang criteria. The estimated values for the elastic constants of CuHgSBr are provided in Table 3, and they satisfy the prerequisites for maintaining elastic stability within the orthorhombic framework.

$$C_{11} > 0 \tag{1}$$

$$C_{11}C_{22} > C_{12}^2 \tag{2}$$

$$C_{11}C_{22}C_{33} + 2C_{12}C_{13}C_{23} \tag{3}$$

$$-C_{11}C_{23}^2 - C_{22}C_{13}^2 - C_{33}C_{12}^2 > 0 \tag{4}$$

$$C_{44} > 0 \tag{5}$$

$$C_{55} > 0 \tag{6}$$

$$C_{66} > 0 \tag{7}$$

Materials with higher values of elastic constants (C_{ij}) are more incompressible and require greater external force to deform them, while materials with lower values of C_{ij} are more easily deformed. Table 4 displayed additional mechanical properties. To understand the internal strains described by equation (8) [52], the Kleinman parameter (ς) was calculated.

$$\varsigma = \frac{C_{11} + 8C_{12}}{7C_{11} + 2C_{12}} \tag{8}$$

Table 3
Elucidated elastic constants and Kleinman parameter (ς) for CuHgSBr using GGA-PBE functional.

XC	C_{11}	C_{22}	C_{33}	C_{44}	C_{55}	C_{66}	C_{12}	C_{13}	C_{23}	ς
GGA-PBE	104.80	102.50	138.66	3.34	4.06	32.93	33.40	44.06	20.82	1.15

The Ϛ provides information about a compound's ability to resist bending and stretching forces. The capacity to withstand alterations in volume when subjected to external pressure is quantified through the bulk modulus. Equations 9–12 [53] can be employed to calculate the bulk modulus, shear modulus, Young's modulus, and Poisson's ratio. The bulk modulus signifies how well a material resists changes in volume, while the shear modulus gauges its resilience to reversible deformations. Young's modulus denotes the material's rigidity against alterations in length. Based on the computed bulk modulus values, CuHgSBr is not considered a hard material. Additionally, the size of the bulk modulus is related to bond distance in the crystal structure, with smaller bond lengths resulting in larger bulk modulus values. In the case of CuHgSBr, the obtained bond lengths are shorter.

$$B = \frac{B_v + B_R}{2} \tag{9}$$

$$G = \frac{G_v + G_R}{2} \tag{10}$$

$$E = \frac{9GB}{3B + G} \tag{11}$$

$$n = \frac{3B - 2G}{6B + 2G} \tag{12}$$

Through the utilization of Pugh's ratio B/G and Poisson's ratio, n, it becomes possible to discern whether a material possesses ductile (ionic) or brittle (covalent) characteristics. A B/G value exceeding 1.75 indicates brittleness, while values below 1.75 suggest ductility. For pure covalent and ionic materials, Poisson's ratio (n) is typically around 0.1–0.25 and 0.25–0.5 [54–56], respectively. Therefore, CuHgSBr can be considered ductile and strongly ionic character. Young's modulus serves as a gauge for determining a material's rigidity. The investigation also covered elastic anisotropy, contributing to the emergence of microcracks. The shear anisotropy ratio concerning (100) shear planes between the (011) and (010) orientations was calculated using equations 13–15 [57]. The calculated shear anisotropy factor values (A_{100}, A_{010}, A_{001}) using the GGA-PBE functional are 0.0860 GPa, 0.0813 GPa, and 0.9375 GPa, respectively. The shear anisotropy ratios A_{100} and A_{001} are both less than 1, indicating the anisotropy nature of CuHgSBr structure. Additionally, A_{010} also have values less than 1.

$$A_{100} = \frac{4C_{44}}{C_{11} + C_{33} - 2C_{13}} \tag{13}$$

$$A_{010} = \frac{4C_{55}}{C_{22} + C_{33} - 2C_{23}} \tag{14}$$

$$A_{001} = \frac{4C_{66}}{C_{11} + C_{22} - 2C_{12}} \tag{15}$$

The orthorhombic structure exhibits elastic anisotropy due to both shear anisotropy and the anisotropy of the linear bulk modulus.

3.4. Optical properties

The evaluation of a material's potential for solar cell and optoelectronic applications necessitates an examination of how the optical properties respond to incident photon radiation [58]. The electronic characteristics of a material are encapsulated in a complex dielectric function, represented by the equation $\epsilon(\omega) = \epsilon_1(\omega) + i\epsilon_2(\omega)$, wherein $\epsilon_1(\omega)$ and $\epsilon_2(\omega)$ stand for the real and imaginary components of the complex dielectric wave function, respectively. Equations 16–20 [59] are employed to compute additional optical properties, including absorption coefficients (α), refractive index n(ω), extinction coefficient κ(ω), reflectivity R(ω), and energy loss function L(ω) (as illustrated in Figs. 6 and 7):

$$\alpha(\omega) = \sqrt{2}\omega \sqrt{\sqrt{\epsilon_1^2(\omega) + \epsilon_2^2(\omega)} - \epsilon_1(\omega)} \tag{16}$$

$$n(\omega) = \left(\frac{\sqrt{\sqrt{\epsilon_1^2(\omega) + \epsilon_2^2(\omega)} + \epsilon_1(\omega)}}{\sqrt{2}} \right) \tag{17}$$

Table 4
Elucidated Bulk modulus (GPa), Young's modulus (GPa), Shear modulus (GPa), Poisson's ratio, and Pugh's ratio for CuHgSBr.

XC	B_v	B_R	B	E_v	E_R	E	G_v	G_R	G	n_v	n_R	n	B/G
GGA-PBE	60.28	59.04	59.66	64.91	22.89	44.75	24.57	7.97	16.27	0.320	0.435	0.374	3.666

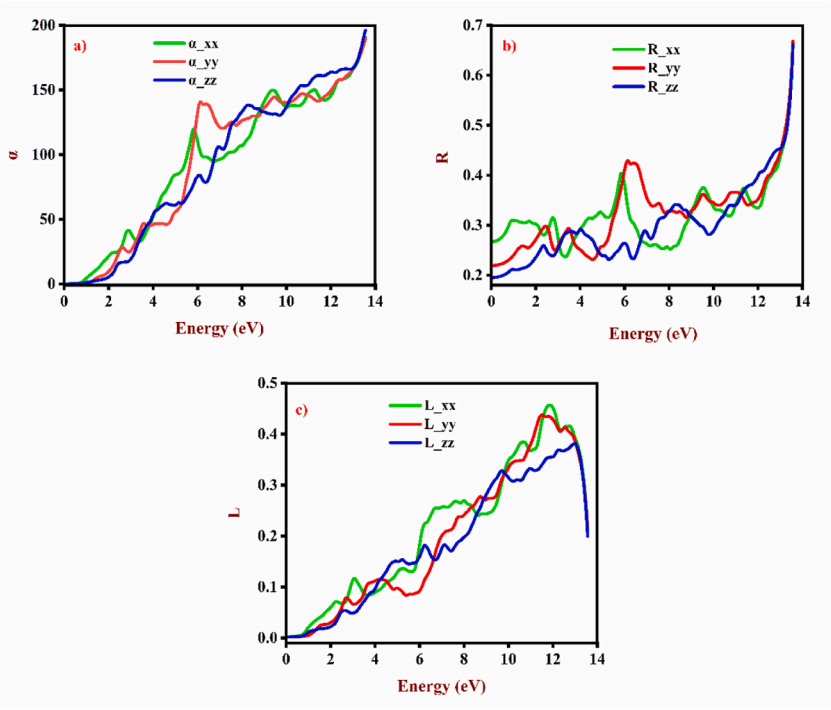

Fig. 6. Estimated a) Absorption coefficient, b) Reflectivity, and c) Energy loss for CuHgSBr.

$$\kappa(\omega) = \left(\frac{\sqrt{\sqrt{\epsilon_1^2(\omega) + \epsilon_2^2(\omega)} - \epsilon_1(\omega)}}{\sqrt{2}} \right) \tag{18}$$

$$L(\omega) = \frac{\epsilon_2(\omega)}{\epsilon_1^2(\omega) + \epsilon_2^2(\omega)} \tag{19}$$

$$R(\omega) = \frac{(n-1)^2 + \kappa^2}{(n+1)^2 + \kappa^2} \tag{20}$$

In crystalline materials, photon absorption is described by the $\epsilon_2(\omega)$ component of the dielectric function. Peaks in $\epsilon_2(\omega)$ are attributed to electronic transitions from the VB to CB. The initiation of absorption in $\epsilon_2(\omega)$ defines the material's bandgap, situated within the visible spectrum, specifically (<3.1 eV for the CuHgSBr compound). This points to robust interband transitions within the material. As a result, CuHgSBr is an attractive material for solar cell applications. Additionally, compared to wide bandgaps, materials with narrow bandgaps enable faster electron transitions.

The CuHgSBr compound displays persistent light absorption across the energy range of 0.8–6 eV, encompassing infrared, visible, and ultraviolet light. This behavior is primarily attributed to the elevated value of the imaginary components $\epsilon_2(\omega)$ in its dielectric function within this energy span along the x, y, and z directions, as illustrated in Fig. 7(b). The static value, commonly known as ϵ_1 (Energy = 0), is the primary characteristic of the $\epsilon_1(\omega)$ curve. In the area of optical and photonic devices, the refractive index n(ω) is a crucial optical parameter to investigate a material's possible uses. The refractive index of the material is correlated to this static value as $n = \sqrt{(\epsilon_1(0))}$. According to Fig. 7(a), the computed values for the static dielectric constant at the zero-frequency limit $\epsilon_1(0)$ are 9.84, 7.62, and 6.67 along x, y and z directions, respectively. At Energy = 0, the $\epsilon_1(\omega)$ graph reaches substantial peak at low energy along x, y, and z regions, which are 0.88 eV, 2.21 eV, and 2.27 eV for CuHgSBr, respectively. Notably, the value exceeding 1 for the y and z directions indicates that the interaction between photons and the material's electrons has caused a reduction in the speed of photons. Photon transmission persists until energy ranges of 5.72–6.38 eV and 8.53–13.56 eV, where the $\epsilon_1(\omega)$ value turned negative. At this energy range, incident photon radiations are believed to be completely absorbed, leading to metallic behavior in the compounds. Similarly, the real component $\epsilon_1(\omega)$ of the dielectric function of CuHgSBr has highest values within the energy range of 0–3 eV, signifying significant electromagnetic wave interaction within this span. The refractive index n(ω) (refer to Fig. 7(c)) achieves its peak values in the same energy range, indicating that electromagnetic waves are largely bent when travelling through the CuHgSBr crystal. The calculated values of static refractive index at the zero-frequency limit n(0) for CuHgSBr along x, y, and z directions are 3.14, 2.76 and 2.58, respectively.

The absorption coefficient serves as a significant optical indicator, providing valuable insights into the absorption of optical energy

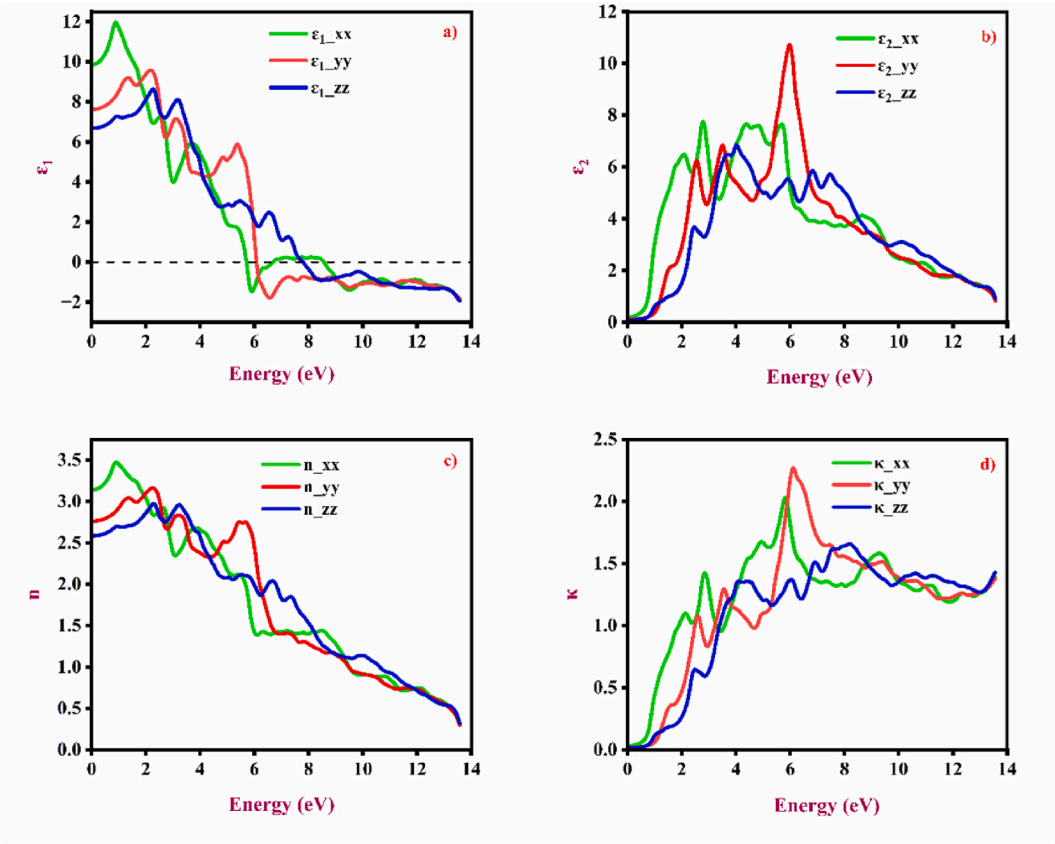

Fig. 7. Calculated a) Real part, b) Imaginary component, c) Refractive index, and d) Extinction coefficient.

per unit length. The absorption process is influenced by the crystal's molecular structure and its band gap. Optical absorption takes place when the frequency of an incoming photon resonates with the transition frequency of an atom. This phenomenon is limited to specific materials due to the frequency-dependent nature of the absorption coefficient. The mechanism behind optical absorption involves electrons transitioning from occupied states in the upper valence band to available unoccupied states in the lower conduction band. As depicted in Fig. 6(a), the absorption rate α(ω) is minimal within the infrared range for energies below 2 eV, indicating the transparency of the CuHgSBr crystal to such light. However, the absorption rate α(ω) experiences a rapid rise from 0.77 eV upwards, reaching its peak values. Notably, incident light parallel to the y-z plane exhibits greater absorption compared to light parallel to the x-axis. The CuHgSBr compound displays higher absorption of ultraviolet light compared to infrared and visible light when energies surpass 9 eV, with diminished directional dependency. The absorption coefficient and the imaginary component of the dielectric function are closely related. The imaginary part of the dielectric function is responsible for describing the absorption of light or other electromagnetic waves in a material. It is represented by a complex number, where the real part accounts for the material's refractive index, and the imaginary part represents the absorption coefficient. In general, the absorption coefficient is directly proportional to the imaginary component of the dielectric function. If there is inconsistency between the absorption coefficient and the imaginary dielectric function, it would imply that the material's absorption behavior is not accurately represented by the dielectric function. The estimated absorption in Fig. 6(a) is not consistent with the imaginary components in the x plane, but it is consistent with y and z plane as shown in Fig. 7(b).

The interaction of fast-moving electrons as they enter substance is governed by two factors: the material's surface behavior, which is managed by reflectivity, and the extent of energy loss, regulated by the energy loss function. Notably, the key reflectivity peaks are consistently located at 13.56 eV in all three spatial directions: x, y, and z are illustrated in Fig. 6(b). According to the loss spectrum in Fig. 6(c), there was no discernible absorption in the visible wavelengths. The largest absorption peak is found in higher energy regions (>10 eV). The decline of electromagnetic wave intensity within the material is explained by the extinction coefficient (κ), as illustrated in Fig. 7(d). The maximum absorption occurs at 5.89 eV, 6.19 eV, and 8.28 eV along x, y, z directions for CuHgSBr, respectively. Based on these optical features, CuHgSBr is a strong contender for photovoltaic and solar cell materials.

3.5. Transport and thermodynamic properties

One direct approach to understanding a material's electronic properties is by employing the concept of effective mass. This measure

is determined by employing a parabolic band approximation, where a polynomial fit of the relationship between wave vector (K) and energy (E) is applied to either the CBM or VBM. Maximum VBM, as depicted in Fig. 8. However, to calculate effective masses precisely, more computationally demanding approaches are needed. The effective mass can be obtained using equation (21), and Table 5 provides the elucidated effective masses expressed with respect to free electron mass.

$$\frac{1}{m_{eff}} = \frac{1}{\hbar^2}\frac{\partial^2 E}{\partial k^2} \tag{21}$$

Furthermore, the breakdown of excitons into electrons (n-type) and holes (p-type) can also be predicted using effective masses and dielectric constants. The binding energy of excitons can be estimated using equation (22) [60], and the values for CuHgSBr are 12.1 meV, 20.2 meV, and 26.4 meV along x, y, and z directions of static dielectric constant. Similarly, the exciton Bohr radius can be estimated using equation (24) [61,62], and the calculated are 60.25 Å, 46.65 Å, and 40.84 Å along x, y, and z directions of static dielectric constant. It is observed that CuHgSBr has a low exciton binding energy in all the three planes, and the value of a^* is greater than the lattice parameters in all the three planes, indicating that it is a weak exciton and falls under Mott-Wannier type.

$$E_b = 13.6\frac{m_\mu}{m_0}\frac{1}{\epsilon_1(0)^2} \tag{22}$$

where, m_μ is reduced effective mass and it is consider using equation (23) [60],

$$\frac{1}{m_\mu} = \frac{1}{m_e^{eff}} + \frac{1}{m_h^{eff}} \tag{23}$$

$$a^* = \epsilon_1(0)\frac{m_0}{m_\mu}a_0 \tag{24}$$

The investigation into the electronic and optical attributes proposes that CuHgSBr holds promise for photovoltaic applications. Due to the global energy crisis, significant research has been dedicated to advanced materials, including smart materials like thermoelectric materials (TE). These possess the capability to convert waste heat into electrical energy and vice versa. A material's thermoelectric performance is heavily influenced by its electronic structure at the VBM. In this study, the transport characteristics of CuHgSBr were simulated using BoltzTraP, a code baser on semi-classical Boltzmann theory. The efficiency of a material in this context is gauged by its elevated electrical conductivity and Seebeck coefficient as well as reduced electronic thermal conductivity.

This study focused on investigating thermoelectric parameters across the temperature range of 50 K–800 K. Various parameters such as electrical conductivity (σ/τ), electronic thermal conductivity (κ_e/τ), lattice thermal conductivity (κ_L), Seebeck coefficient (S), Power factor (P.F), and figure of merit (ZT) for CuHgSBr were calculated. The computed electrical conductivity (σ/τ) is depicted in Fig. 9(a), illustrating a rise in σ/τ values as temperature increases. As materials display enhanced semiconducting properties, their electrical conductivity also increases, enabling electrons to surmount the fermi level barrier. For CuHgSBr, the σ/τ values are 4.24×10^{16} (1/Ω cm s) at 50 K and 5.73×10^{18} (1/Ω cm s) at 800 K.

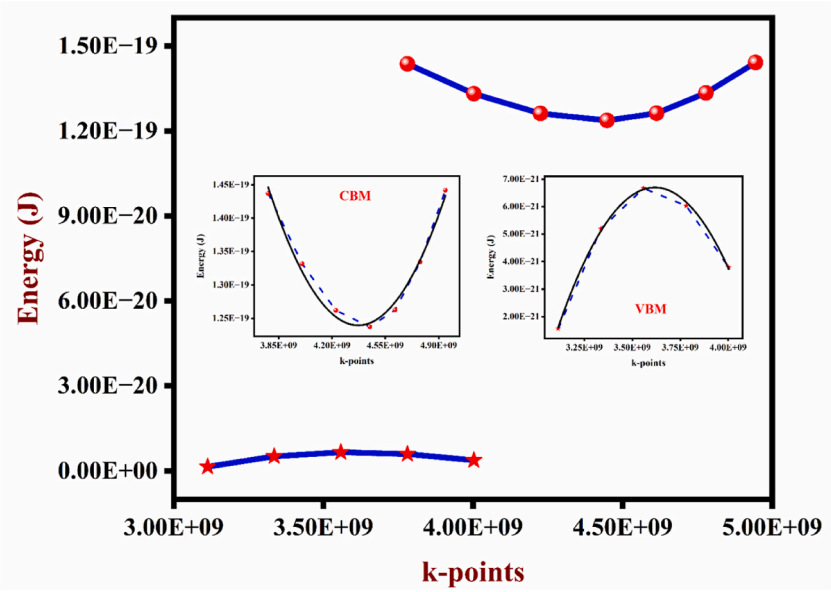

Fig. 8. Calculated quadric curve of VBM and CBM for CuHgSBr.

Table 5
Calculated effective mass of electron and effective mass of hole for CuHgSBr.

Compound	Electron	Hole
CuHgSBr	0.1210 m_e	0.3025 m_e

The thermopower (S) of CuHgSBr, depicted in Fig. 9(b), displays a consistently positive trend across the entire temperature range, indicating a p-type characteristic of the compound. The computed values of S at 50 K and 800 K are 317 (μV/K) and 198 (μV/K), respectively. The higher Seebeck coefficient (S) at 50 K results from the presence of flat bands at the VB. As temperature increases, S significantly decreases, as depicted in Fig. 9(b). The electronic component of thermal conductivity (κ_e/τ) is depicted in Fig. 9(c), demonstrating a gradual increase with rising temperature. The κ_e/τ values at 50 K and 800 K are 2.48×10^{11} (W/mKs) and 3.20×10^{14} (W/mKs), respectively.

Power factor (P.F), which combines electrical conductivity and Seebeck coefficient, serves as an efficiency descriptor for thermoelectric materials. Fig. 10(a) depicts the fluctuation of power factor with temperature. The lattice thermal conductivity (κ_L) was estimated using the Slack [63] equation (25), and the values are presented in Fig. 9(d).

$$\kappa_l = A\frac{M_a\theta^3\delta}{\gamma^2 Tn^{2/3}} \tag{25}$$

where, A, θ, and γ, are represented as constant, Debye temperature, and Grüneisen parameter. The constant A can be calculated using equation (26).

$$A = \frac{2.43 \times 10^{-8}}{1 - \frac{0.514}{\gamma} + \frac{0.228}{\gamma^2}} \tag{26}$$

The value of θ and γ are 183.84 K and 2.35 calculated using IR-Elast code, which is incorporated in WIEN2k package. The tendency of κ_L shows that as the temperature rises, heat transfer of phonon decreases. The κ_L values at 50 K and 800 K are 1.77 (W/mK) and 0.11 (W/mK), respectively, while the computed lattice thermal conductivity at 300 K is 0.29 (W/mK) as shown in Fig. 9(d).

Figure of merit (ZT), a widely-used transport parameter, assesses material effectiveness. As shown in Fig. 10(b), a higher ZT indicates greater suitability for thermoelectric applications, necessitating elevated electrical conductivity, Seebeck coefficient, and diminished thermal conductivity. In this study, the calculated figure of merit (ZT) for CuHgSBr at 50 K and 800 K are 0.0012 and 0.54, respectively, indicating an increase with temperature. This behavior is attributed to the flat band structure at the upper VB.

In conclusion, the band gap significantly influences a material's electrical conductivity, with CuHgSBr's properties affected by its unique band gap chemistry. With an increasing temperature, the figure of merit (ZT) also increases, making CuHgSBr a suitable candidate for thermoelectric applications. Furthermore, the temperature-dependent thermodynamic characteristics such as free energy F, entropy S, and heat capacity C_v were estimated using the harmonic approximation in the phonopy [64], interfaced using WIEN2k, as shown in Fig. 11. As temperature climbs, free energy decreases, while entropy and heat capacity increase in accordance with the third law of thermodynamics. CuHgSBr's heat capacity adheres to the T^3 equation of the Debye model [65] at low temperatures, rapidly increasing up to 300 K. at higher temperatures, fluctuation diminishes, consistent with the Dulong-Petit rule [66].

4. Conclusion

To sum up, we conducted a comprehensive analysis of various properties including structural, electronic, elastic, optical, thermodynamic, and transport properties of the CuHgSBr quaternary compound using the Density Functional Theory (DFT) within the WIEN2k software. The optimized lattice constants were determined as a = 10.137, b = 18.517, c = 4.042 Å for CuHgSBr. Additionally, the bandgap was calculated to be 0.76 eV. Based on the results of the elastic constants, CuHgSBr was determined to be ductile (ionic), and mechanically stable at relatively low pressure, indicating its potential for use in resilient materials. Moreover, our studied compound shows promise for photovoltaic applications due to its predicted bandgap, high refractive index, and high absorption coefficient, particularly in the Ultra-violet to visible regions of the electromagnetic spectrum. Furthermore, we employed the semi-classical BoltzTrap code to compute the thermoelectric features of CuHgSBr. By fitting the band structure as VBM and CBM, we obtained the effective mass and exciton binding energy. Our analysis reveals the presence of a Mott-Wannier type exciton based on the exciton Bohr radius. Remarkably, CuHgSBr exhibits strong potential as a thermoelectric material, supported by power factor and ZT outcomes. These results are promising, driving us to delve deeper into the intricate and captivating domain of chalcogenide crystals in this field. In the context of future directions, we anticipate exploring methods to reduce thermal conductivities to further enhance the thermoelectric performance of CuHgSBr. The investigation of CuHgSBr as two-dimensional (2D) and one-dimensional (1D) materials could offer substantial improvements in this aspect. Advancements in DFT computations, such as employing potentials like the Becke-Johnson or hybrid potentials, hold promise for upcoming research endeavours. Ultimately, we foresee an ongoing focus on optimizing CuHgSBr's properties and envision its potential applications in various dimensions.

Author contribution statement

M. Hariharan: Analysed and interpreted the data; performed the experiments; wrote the paper.

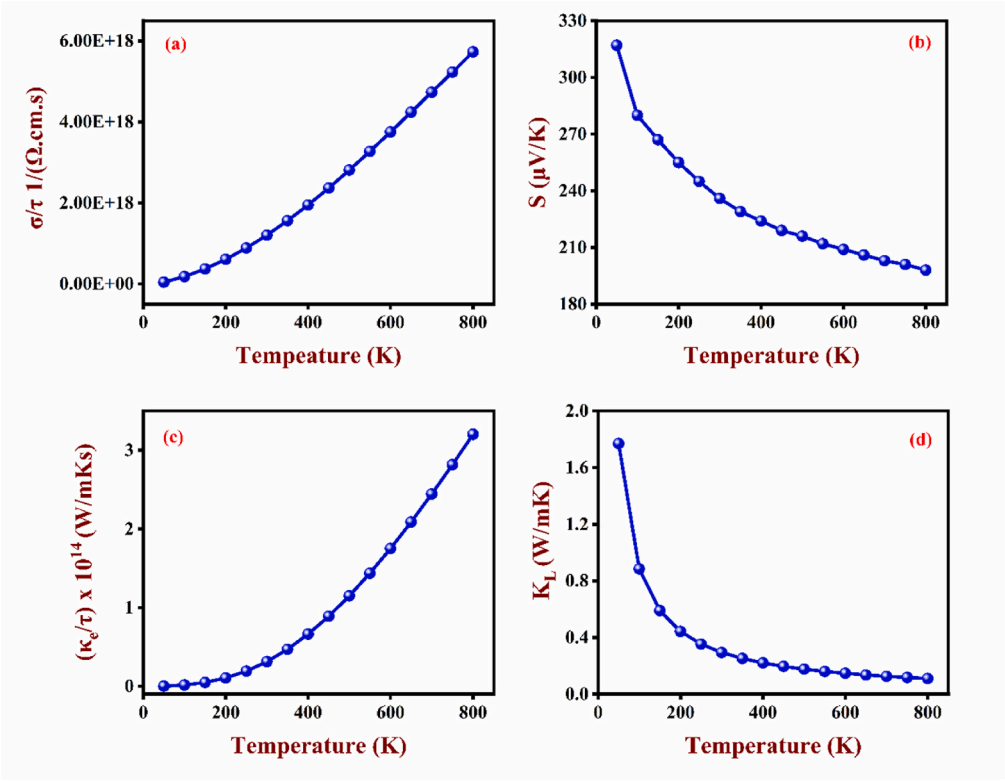

Fig. 9. Calculated a) electrical conductivity, b) Seebeck coefficient, c) and d) electronic and lattice thermal conductivities.

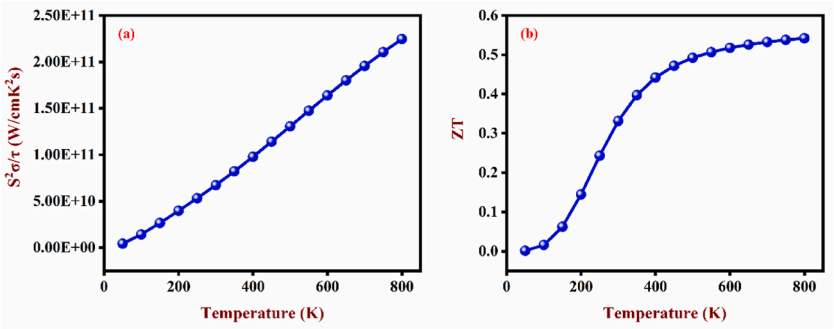

Fig. 10. Calculated a) Power factor and b) Figure of merit (ZT).

R. D. Eithiraj: Conceived and designed the experiments; contributed regents, material, analysis tools or data; wrote the paper.

Date availability statement

All data that support the findings of this study are available from the corresponding author upon reasonable request.

Additional information

No additional information is available for this paper.

Declaration of competing interest

The authors declare that they have no known competing financial interests or personal relationships that could have appeared to influence the work reported in this paper.

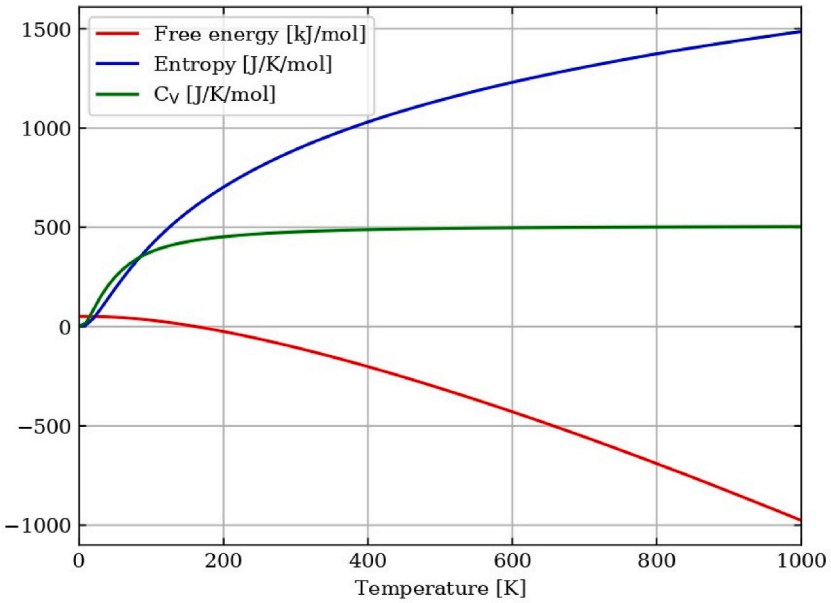

Fig. 11. Estimated thermodynamic properties of CuHgSBr.

References

[1] Jian He, Terry M. Tritt, Advances in thermoelectric materials research: looking back and moving forward, Science 357 (6358) (2017), eaak9997, https://doi.org/10.1126/science.aak9997.

[2] David Michael Rowe (Ed.), CRC Handbook of Thermoelectrics, CRC press, 2018.

[3] David Michael Rowe (Ed.), Thermoelectrics Handbook: Macro to Nano, CRC press, 2018.

[4] Jing-Feng Li, Wei-Shu Liu, Li-Dong Zhao, Min Zhou, High-performance nanostructured thermoelectric materials, NPG Asia Mater. 2 (4) (2010) 152–158, https://doi.org/10.1038/asiamat.2010.138.

[5] Xiao Zhang, Li-Dong Zhao, Thermoelectric materials: energy conversion between heat and electricity, Journal of Materiomics 1 (2) (2015) 92–105, https://doi.org/10.1016/j.jmat.2015.01.001.

[6] Li-Dong Zhao, Vinayak P. Dravid, Mercouri G. Kanatzidis, The panoscopic approach to high performance thermoelectrics, Energy Environ. Sci. 7 (1) (2014) 251–268, https://doi.org/10.1039/C3EE43099E.

[7] Jihui Yang, Thierry Caillat, Thermoelectric materials for space and automotive power generation, MRS Bull. 31 (3) (2006) 224–229, https://doi.org/10.1557/mrs2006.49.

[8] Richard R. Furlong, Earl J. Wahlquist, US space missions using radioisotope power systems, Nucl. News 42 (1999) 26–35.

[9] Sahib Hasan, Saro San, Khagendra Baral, Neng Li, Rulis Paul, Ching Wai-Yim, First-principles calculations of thermoelectric transport properties of quaternary and ternary bulk chalcogenide crystals, Materials 15 (8) (2022) 2843, https://doi.org/10.3390/ma15082843.

[10] Muhammad Irfan, Sikander Azam, Alaa Dahshan, Issam El Bakkali, Khalid Nouneh, First-principles study of opto-electronic and thermoelectric properties of $SrCdSnX_4$ (X= S, Se, Te) alkali metal chalcogenides, Computational Condensed Matter 30 (2022), e00625, https://doi.org/10.1016/j.cocom.2021.e00625.

[11] Min-Ling Liu, I-Wei Chen, Fu-Qiang Huang, Li-Dong Chen, Improved thermoelectric properties of Cu-doped quaternary chalcogenides of $Cu_2CdSnSe_4$, Adv. Mater. 21 (37) (2009) 3808–3812, https://doi.org/10.1002/adma.200900409.

[12] C. Sevik, T. Çağın, Ab initio study of thermoelectric transport properties of pure and doped quaternary compounds, Phys. Rev. B 82 (4) (2010), 045202, https://doi.org/10.1103/PhysRevB.82.045202.

[13] Maria Ibáñez, Reza Zamani, Aaron LaLonde, Doris Cadavid, Wenhua Li, Alexey Shavel, Jordi Arbiol, et al., $Cu_2ZnGeSe_4$ nanocrystals: synthesis and thermoelectric properties, J. Am. Chem. Soc. 134 (9) (2012) 4060–4063, https://doi.org/10.1021/ja211952z.

[14] Wolfgang G. Zeier, Christophe P. Heinrich, Tristan Day, Chatr Panithipongwut, Gregor Kieslich, Brunklaus Gunther, G. Jeffrey Snyder, Wolfgang Tremel, Bond strength dependent superionic phase transformation in the solid solution series $Cu_2ZnGeSe_{4-x}S_x$, J. Mater. Chem. A 2 (6) (2014) 1790–1794, https://doi.org/10.1039/C3TA13007J.

[15] J. Navrátil, V. Kucek, T. Plecháček, E. Černošková, F. Laufek, Č. Drašar, P. Knotek, Thermoelectric properties of $Cu_2HgSnSe_4$-$Cu_2HgSnTe_4$ solid solution, J. Electron. Mater. 43 (2014) 3719–3725, https://doi.org/10.1007/s11664-014-3075-8.

[16] Subhajit Roychowdhury, Tanmoy Ghosh, Raagya Arora, Manisha Samanta, Lin Xie, Niraj Kumar Singh, Ajay Soni, Jiaqing He, Umesh V. Waghmare, Kanishka Biswas, Enhanced atomic ordering leads to high thermoelectric performance in $AgSbTe_2$, Science 371 (6530) (2021) 722–727, https://doi.org/10.1126/science.abb3517.

[17] Min Hong, Zhi-Gang Chen, Lei Yang, Zhi-Ming Liao, Yi-Chao Zou, Yan-Hui Chen, Syo Matsumura, Jin Zou, Achieving zT> 2 in p-type $AgSbTe_{2-x}Se_x$ alloys via exploring the extra light valence band and introducing dense stacking faults, Adv. Energy Mater. 8 (9) (2018), 1702333, https://doi.org/10.1002/aenm.201702333.

[18] Shuping Deng, Xianyan Jiang, Ziye Zhang, Junjie Liu, Lili Chen, Ning Qi, Xinfeng Tang, Yichu Wu, Zhiquan Chen, Structural features and thermoelectric performance of chalcopyrite Cu (In, Ga) Te_2 system by isoelectronic substitution, Curr. Appl. Phys. 26 (2021) 24–34, https://doi.org/10.1016/j.cap.2021.03.013.

[19] Yaqiong Zhong, Debalaya Sarker, Tao Fan, Liangliang Xu, Li Xie, Guang-Zhao Qin, Zhong-kang han, and jiaolin cui, computationally guided synthesis of high performance thermoelectric materials: defect engineering in $AgGaTe_2$, Advanced Electronic Materials 7 (4) (2021), 2001262, https://doi.org/10.1002/aelm.202001262.

[20] Muchtar, Rifqi Ahmad, Bhuvanesh Srinivasan, Sylvain Le Tonquesse, Saurabh Singh, Nugroho Soelami, Brian Yuliarto, David Berthebaud, Takao Mori, Physical insights on the lattice softening driven mid-temperature range thermoelectrics of Ti/Zr-inserted SnTe—an outlook beyond the horizons of conventional phonon scattering and excavation of heikes' equation for estimating carrier properties, Adv. Energy Mater. 11 (28) (2021), 2101122, https://doi.org/10.1002/aenm.202101122.

[21] Tristan Barbier, Bhuvanesh Srinivasan, David Berthebaud, Volker Eyert, Raymond Frésard, Rodolphe Macaigne, Sylvain Marinel, Oleg I. Lebedev, Emmanuel Guilmeau, Maignan Antoine, Structural study and evaluation of thermoelectric properties of single-phase isocubanite ($CuFe_2S_3$) synthesized via an ultra-fast efficient microwave radiation technique, Sustain. Energy Fuels 5 (22) (2021) 5804–5813, https://doi.org/10.1039/D1SE01007G.

[22] Sikander Azam, Saleem Ayaz Khan, Minar Jan, Wilayat Khan, Haleem Ud Din, Rabah Khenata, Ghulam Murtaza, Saad Bin-Omran, Souraya Goumri-Said, Coulomb interaction and spin-orbit coupling calculations of thermoelectric properties of the quaternary chalcogenides Tl_2PbXY_4 (X= Zr, Hf and Y= S, Se), Semicond. Sci. Technol. 30 (10) (2015), 105018, https://doi.org/10.1088/0268-1242/30/10/105018.

[23] A.O. Selezen, I.D. Olekseyuk, G.L. Myronchuk, O.V. Smitiukh, L.V. Piskach, Synthesis and structure of the new semiconductor compounds $Tl_2BIIDIVX_4$ (BII–Cd, Hg; DIV–Si, Ge; X–Se, Te) and isothermal sections of the Tl_2Se–CdSe-Ge (Sn) Se_2 systems at 570 K, J. Solid State Chem. 289 (2020), 121422, https://doi.org/10.1016/j.jssc.2020.121422.

[24] Tuan V. Vu, A.A. Lavrentyev, B.V. Gabrelian, A.O. Selezen, L.V. Piskach, G.L. Myronchuk, M. Denysyuk, V.A. Tkach, Khang D. Pham, O.Y. Khyzhun, Crystal growth, electronic and optical properties of $Tl_2CdSnSe_4$, a recently discovered prospective semiconductor for application in thin film solar cells and optoelectronics, Opt. Mater. 111 (2021), 110656, https://doi.org/10.1016/j.optmat.2020.110656.

[25] M. Yu Mozolyuk, L.V. Piskach, A.O. Fedorchuk, I.D. Olekseyuk, O.V. Parasyuk, Physico-chemical interaction in the Tl_2Se–HgSe–$DIVSe_2$ systems (DIV–Si, Sn), Mater. Res. Bull. 47 (11) (2012) 3830–3834, https://doi.org/10.1016/j.materresbull.2012.03.056.

[26] A.A. Lavrentyev, B.V. Gabrelian, Tuan V. Vu, L.N. Ananchenko, G.L. Myronchuk, O.V. Parasyuk, V.A. Tkach, K.I. Kopylova, Oleg Yu Khyzhun, Electronic and optical properties of quaternary sulfide Tl_2HgSnS_4, a promising optoelectronic semiconductor: a combined experimental and theoretical study, Opt. Mater. 92 (2019) 294–302, https://doi.org/10.1016/j.optmat.2019.04.032.

[27] Johannes Beck, Matthias Rompel, Über Münzmetall-Quecksilber-Chalkogenidhalogenide, II Hydrothermalsynthese, Kristallstruktur und Phasenumwandlung von CuHgSCl und CuHgSBr, Z. Anorg. Allg. Chem. 629 (3) (2003) 421–428, https://doi.org/10.1002/zaac.200390070.

[28] M. Guillo, B. Mercey, A. Deschanvres, Systemes CuX (X= Cl, Br) HgS. etude des composes CuHgSX (X= Cl, Br), Mater. Res. Bull. 14 (7) (1979) 947–954, https://doi.org/10.1016/0025-5408(79)90162-4.

[29] Johannes Beck, Hans-Lothar Keller, Matthias Rompel, Lars Wimbert, Hydrothermalsynthese und Kristallstruktur der Münzmetall-Quecksilber-Chalkogenidhalogenide CuHgSeBr, AgHgSBr und AgHgSI, Z. Anorg. Allg. Chem. 627 (9) (2001) 2289–2294, https://doi.org/10.1002/15213749(200109)627:9%3C2289::AIDZAAC2289%3E3.0.CO;2-E.

[30] Peter Blaha, Karlheinz Schwarz, Georg KH. Madsen, Dieter Kvasnicka, Joachim Luitz, wien2k, An augmented plane wave+ local orbitals program for calculating crystal properties 60 (1) (2001).

[31] J.P. Perdew, E.R. McMullen, Alex Zunger, Density-functional theory of the correlation energy in atoms and ions: a simple analytic model and a challenge, Phys. Rev. 23 (6) (1981) 2785, https://doi.org/10.1103/PhysRevA.23.2785.

[32] Morteza Jamal, M. Bilal, Iftikhar Ahmad, S. Jalali-Asadabadi, IRelast package, J. Alloys Compd. 735 (2018) 569–579, https://doi.org/10.1016/j.jallcom.2017.10.139.

[33] Georg KH. Madsen, David J. Singh, BoltzTraP. A code for calculating band-structure dependent quantities, Comput. Phys. Commun. 175 (1) (2006) 67–71, https://doi.org/10.1016/j.cpc.2006.03.007.

[34] Hongliang Shi, David Parker, Mao-Hua Du, David J. Singh, Connecting thermoelectric performance and topological-insulator behavior: Bi_2Te_3 and Bi_2Te_2Se from first principles, Phys. Rev. Appl. 3 (1) (2015), 014004, https://doi.org/10.1103/PhysRevApplied.3.014004.

[35] D.P. Young, C.L. Brown, P. Khalifah, R.J. Cava, A.P. Ramirez, Thermoelectric properties of Ag_3AuTe_2, J. Appl. Phys. 88 (9) (2000) 5221–5224, https://doi.org/10.1063/1.1316057.

[36] T. Van Quang, Valance band maximum and thermoelectric properties of Bi2O2Se: first Principle Calculations, Commun. Phys. 30 (3) (2020) 267–278, https://doi.org/10.15625/0868-3166/30/3/14958.

[37] A. Ghafari, K. Habicht, Electronic structure and transport properties of $TlInSe_2$ and $Tl_{0.5}Li_{0.5}InSe_2$, Mater. Today Energy 12 (2019) 95–106, https://doi.org/10.1016/j.mtener.2018.12.005.

[38] Zheng Liu, Feng Liu, Yong-Shi Wu, Exotic electronic states in the world of flat bands: from theory to material, Chin. Phys. B 23 (7) (2014), 077308, https://doi.org/10.1088/1674-1056/23/7/077308.

[39] William R. Meier, Mao-Hua Du, Satoshi Okamoto, Narayan Mohanta, Andrew F. May, Michael A. McGuire, Craig A. Bridges, German D. Samolyuk, Brian C. Sales, Flat bands in the CoSn-type compounds, Phys. Rev. B 102 (7) (2020), 075148, https://doi.org/10.1103/PhysRevB.102.075148.

[40] Leon Balents, Cory R. Dean, Dmitri K. Efetov, Andrea F. Young, Superconductivity and strong correlations in moiré flat bands, Nat. Phys. 16 (7) (2020) 725–733, https://doi.org/10.1038/s41567-020-0906-9.

[41] P.R. Mammadli, Physico-chemical interaction of the copper and antimony iodides, Azerbaijan Chemical Journal 1 (2021) 43–47.

[42] Haiying He, Roberto Orlando, Miguel A. Blanco, Ravindra Pandey, Emilie Amzallag, Isabelle Baraille, Michel Rérat, First-principles study of the structural, electronic, and optical properties of Ga_2O_3 in its monoclinic and hexagonal phases, Phys. Rev. B 74 (19) (2006), 195123, https://doi.org/10.1103/PhysRevB.74.195123.

[43] I. Hase, T. Yanagisawa, K. Kawashima, Computational design of flat-band material, Nanoscale Res. Lett. 13 (2018) 1–5, https://doi.org/10.1186/s11671-018-2464-y.

[44] Oleg Derzhko, Johannes Richter, Mykola Maksymenko, Strongly correlated flat-band systems: the route from Heisenberg spins to Hubbard electrons, Int. J. Mod. Phys. B 29 (12) (2015), 1530007, https://doi.org/10.1142/S0217979215300078.

[45] Sajid Khan, Rashid Ahmad, Nasir Mehmood, Faryal Hina, Alatf Ur Rehman, Shams U. Zaman, H.J. Kim, First-principles investigation of the physical properties of indium based fluoroperovskites $InAF_3$ (A= Ca, Cd and Hg), Mater. Sci. Semicond. Process. 121 (2021), 105385, https://doi.org/10.1016/j.mssp.2020.105385.

[46] David J. Singh, Doping-dependent thermopower of PbTe from Boltzmann transport calculations, Phys. Rev. B 81 (19) (2010), 195217, https://doi.org/10.1103/PhysRevB.81.195217.

[47] David Parker, David J. Singh, Thermoelectric properties of $AgGaTe_2$ and related chalcopyrite structure materials, Phys. Rev. B 85 (12) (2012), 125209, https://doi.org/10.1103/PhysRevB.85.125209.

[48] Jun-Won Rhim, Bohm-Jung Yang, Singular flat bands, Adv. Phys. X 6 (1) (2021), 1901606, https://doi.org/10.1080/23746149.2021.1901606.

[49] Enamul Haque, M. Anwar Hossain, First-principles study of elastic, electronic, thermodynamic, and thermoelectric transport properties of TaCoSn, Results Phys. 10 (2018) 458–465, https://doi.org/10.1016/j.rinp.2018.06.053.

[50] Félix Mouhat, François-Xavier Coudert, Necessary and sufficient elastic stability conditions in various crystal systems, Phys. Rev. B 90 (22) (2014), 224104, https://doi.org/10.1103/PhysRevB.90.224104.

[51] Max Born, Kun Huang, M. Lax, Dynamical theory of crystal lattices, Am. J. Phys. 23 (7) (1955), 474-474.

[52] Leonard Kleinman, "Deformation potentials in silicon. I. Uniaxial strain, Phys. Rev. 128 (6) (1962) 2614, https://doi.org/10.1103/PhysRev.128.2614.

[53] Richard Hill, The elastic behaviour of a crystalline aggregate, Proc. Phys. Soc. 65 (5) (1952) 349, https://doi.org/10.1088/0370-1298/65/5/307.

[54] Mwende Mbilo, George S. Manyali, Robinson J. Musembi, Ab initio study of $K_3Cu_3P_2$ material for photovoltaic applications, Computational Condensed Matter 32 (2022), e00726, https://doi.org/10.1016/j.cocom.2022.e00726.

[55] M.I. Naher, S.H. Naqib, First-principles insights into the mechanical, optoelectronic, thermophysical, and lattice dynamical properties of binary topological semimetal $Baga_2$, Results Phys. 37 (2022), 105507, https://doi.org/10.1016/j.rinp.2022.105507.

[56] D.V. Suetin, I.R. Shein, A.L. Ivanovskii, Elastic and electronic properties of hexagonal and cubic polymorphs of tungsten monocarbide WC and mononitride WN from first-principles calculations, Phys. Status Solidi 245 (8) (2008) 1590–1597, https://doi.org/10.1002/pssb.200844077.

[57] Viggo Tvergaard, John W. Hutchinson, Microcracking in ceramics induced by thermal expansion or elastic anisotropy, J. Am. Ceram. Soc. 71 (3) (1988) 157–166, https://doi.org/10.1111/j.1151-2916.1988.tb05022.x.

[58] Rahul Bhattacharjee, Surya Chattopadhyaya, Effects of barium (Ba) doping on structural, electronic and optical properties of binary strontium chalcogenide semiconductor compounds-A theoretical investigation using DFT based FP-LAPW approach, Mater. Chem. Phys. 199 (2017) 295–312, https://doi.org/10.1016/j.matchemphys.2017.06.057.
[59] Muhammad Shahzad Yaseen, Jifeng Sun, Hanjun Fang, G. Murtaza, David S. Sholl, First-principles study of electronic and optical properties of ternary compounds $AuBX_2$ (X= S, Se, Te) and $AuMTe_2$ (M= Al, In, Ga), Solid State Sci. 111 (2021), 106508, https://doi.org/10.1016/j.solidstatesciences.2020.106508.
[60] Chol-Jun Yu, Advances in modelling and simulation of halide perovskites for solar cell applications, J. Phys.: Energy 1 (2) (2019), 022001, https://doi.org/10.1088/2515-7655/aaf143.
[61] Un-Gi Jong, Yu Chol-Jun, Ri Jin-Song, Nam-Hyok Kim, Ri Guk-Chol, Influence of halide composition on the structural, electronic, and optical properties of mixed CH_3NH_3Pb $(I_{1-x}Br_x)_3$ perovskites calculated using the virtual crystal approximation method, Phys. Rev. B 94 (12) (2016), 125139, https://doi.org/10.1103/PhysRevB.94.125139.
[62] Anupriya Nyayban, Subhasis Panda, Avijit Chowdhury, B. Indrajit Sharma, First principle studies of rubidium lead halides towards photovoltaic application, Mater. Today Commun. 24 (2020), 101190, https://doi.org/10.1016/j.mtcomm.2020.101190.
[63] Donald T. Morelli, Glen A. Slack, High lattice thermal conductivity solids, in: High Thermal Conductivity Materials, NY Springer New York, New York, 2006, pp. 37–68.
[64] Atsushi Togo, First-principles phonon calculations with phonopy and phono3py, J. Phys. Soc. Jpn. 92 (1) (2023), 012001, https://doi.org/10.7566/JPSJ.92.012001.
[65] Peter Debye, Zur theorie der spezifischen wärmen, Ann. Phys. 344 (14) (1912) 789–839, https://doi.org/10.1002/andp.19123441404.
[66] A.T. Petit, P.L. Dulong, Research on some important points of the theory of heat, Ann. Chem. Phys. 10 (1981) 395–413.